Journal of Thermal Science Vol.34, No.2 (2025) 542−554

https://doi.org/10.1007/s11630-024-2063-4 **Article ID: 1003-2169(2025)02-0542-13**

Effects of Operation Parameters on Heat Transfer in Tubular Moving Bed Heat Exchangers: A CFD-DEM Study

LU Weiqin[1], LI Zhihan[2], TANG Xueyu[1], LIU Dinghe[3], KE Xiwei[1], ZHOU Tuo[1*]

1. Key Laboratory for Thermal Science and Power Engineering of Ministry of Education, Department of Energy and Power Engineering, Tsinghua University, Beijing 100084, China
2. School of Transportation and Vehicle Engineering, Shandong University of Technology, Ji'nan 255049, China
3. College of Electrical and Power Engineering, Taiyuan University of Technology, Taiyuan 030024, China

Abstract: Tubular moving bed heat exchangers (MBHEs) present inherent advantages for efficiently and stably recovering sensible heat from high-temperature granular bulk. In this study, we introduce a viable and practical approach based on the combined approach of Computational Fluid Dynamics with Discrete Element Method (CFD-DEM) and employ it to conduct a comprehensive investigation into the effects of operation parameters on tubular MBHEs. These parameters include inlet particle temperature (ranging from 500°C to 700°C), tube wall temperature (ranging from 50°C to 250°C), and particle descent velocity (ranging from 0.5 mm/s to 12 mm/s). Our analysis reveals that the heat radiation and gas film heat conduction predominantly govern the heat transfer process in the particle-fluid-wall system, collectively contributing to approximately 90% of the total heat flux of tube wall ($Q_{\mathrm{w}}^{\mathrm{simu}}$). The results indicate that increasing the inlet particle temperature and reducing the tube wall temperature intensify heat transfer by enlarging the temperature difference. More interestingly, $Q_{\mathrm{w}}^{\mathrm{simu}}$ exhibits three distinct stages as particle descent velocity increases, including an ascent stage, a descent stage, and a stable stage. Furthermore, the simulation attempts suggest that the optimal descent velocity for maximizing $Q_{\mathrm{w}}^{\mathrm{simu}}$ falls within the range of 1.3–2.0 mm/s. These findings not only uncover the precise influence mechanisms of operation parameters on heat transfer outcomes but also offer valuable insights for heat transfer enhancement efficiency in MBHE system.

Keywords: tubular moving bed heat exchangers; heat transfer; operation parameters; CFD-DEM; heat transfer enhancement

1. Introduction

Millimeter or even centimeter-sized particles, such as iron sintered pellets and blast furnace slag, as well as exhaust gases, are prevalent by-products in energy-intensive industries. These materials carry substantial heat content, emphasizing the immense potential of waste heat recovery in such industries [1–4] through the utilization of heat exchangers. Among various heat exchanger technologies, the MBHEs have emerged as a focal point due to their high compactness, acceptable heat loss, low costs, and preferable capacities to operate continuously as well as to handle solid particles [5].

Received: Apr 22, 2024 AE: YAN Suying Corresponding author: ZHOU Tuo E-mail: zhoutuo@mail.tsinghua.edu.cn

Nomenclature

A_i	Area/m^2	T	Time/s
b_f	Fluid bulk viscosity/Pa·s	V	Poisson's ratio
C_D	Drag coefficient	v_p/v_f	Particle or fluid Velocity vector/m·s^{-1}
C_p	Specific heat capacity/J·(kg·K)$^{-1}$	**Greek letters**	
d_p	Particle diameter/m	α	Normal overlap quantity/m
E	Young's modulus/Pa	α_f	Volume fraction occupied by the fluid
E_f	Fluid energy/J	β	A constant equal to $-(\ln e)/\sqrt{\ln^2 e+\pi^2}$
$\boldsymbol{F}$	Force vector/N	δ	Gas film thickness/m
F_{ij}	View factor	δ_{ol}	Amount of overlap/m
F_{pp}/F_{pw}	Correction factor for artificial softening	ε	Emissivity
G	Elastic modulus/Pa	η_p/η_w	Roughness of particle surface or wall surface/m
$\boldsymbol{g}$	Gravitational acceleration/m·s^{-2}	λ_f	Fluid thermal conductivity/W·(m·K)$^{-1}$
HF_x	Heat flux of tube wall/W	μ_f	Fluid shear viscosity/Pa·s
h_f	Fluid enthalpy/J·kg^{-1}	μ_r	Coefficient of rolling friction
$\overline{\overline{\boldsymbol{I}}}$	Identity matrix	μ_s	Coefficient of static friction
I_p	Moment of particle inertia/m^4	ρ	Density/kg·m^{-3}
K_{pf}	Drag function/kg·s^{-1}	σ	Stefan-Boltzmann constant, 5.67×10^{-8} W·(m^2·K^4)$^{-1}$
K	Thermal conductivity/W·(m·K)$^{-1}$	$\boldsymbol{\tau}$	Tolling friction torque vector/N·m
L	Characteristic length/m	$\overline{\overline{\boldsymbol{\tau}}}_f$	Fluid stress-strain tensor
l_{ij}	Contact distance/m	$\boldsymbol{\tau}_p$	Total torque vector of the particle/N·m
m_p	Particle mass/kg	$\boldsymbol{\omega}$	Angular velocity vector/rad·s^{-1}
Nu	Nusselt number	**Abbreviations**	
p_f	Fluid pressure/Pa	CFD-DEM	Combined approach of computational fluid mechanics and discrete element method
Pr	Prandtl number	DEM	Discrete element method
Q	Heat flux/W	F-P	Fluid-to-particle
R,r	Particle radius/m	F-W	Fluid-to-wall
Re_p	Particle Reynolds number	MBHE	Moving bed heat exchanger
S_n,S_t	Normal or shear stiffness/N·m^{-1}	P-P	Particle-to-particle
T_p,T_f	Particle or fluid temperature/K	P-W	Particle-to-wall
ΔT	Temperature difference/K	TFM	Two-fluid method

To our knowledge, MBHEs can be categorized into typical ones, plate-shell ones, and tubular ones according to their geometry configuration. In typical MBHEs, particles are driven by gravity or mechanical forces, move slowly or remain relatively stationary (the annular cooler and the belt cooler [6–8]). Gas, typically air, acted as the heat transfer medium, flows through a porous medium composed of high temperature particles at a specific velocity. In this process, gas undergoes sensible heat exchange via gas-solid heat convection. Then, the heated gas can be utilized as an energy source input for the waste heat boiler [2], combustion air supply, and other industrial processes. Besides, the latter two types (plate-shell and tubular) are equipped with internal heat exchangers: in plate-shell MBHEs, plates or shells are used [9], while in tubular MBHEs, tube banks or tube bundles are used [2]. The working medium, typically water, flows through the heat exchanger and undergoes heat exchange with the particles on the opposing side of the wall. In the realm of waste heat recovery, particularly concerning large particles, the tubular MBHE presents inherent advantages because of its well-established and dependable waste heat recovery capability, coupled with higher energy efficiency compare conventional models. Furthermore, it exhibits enhanced capacity for managing relatively large particles, surpassing that of plate-shell configurations.

As far as we know, researches on tubular MBHEs predominantly focused on investigating various aspects. These include studying particle flow patterns and heat

transfer characteristics around individual tube [10], corresponding influence factors [11], as well as approaches to enhance heat and mass transfer [12]. Due to the high coupling property of heat and mass transfer, discussions often intertwined these aspects. Researchers have found that there are two evident features of particle flow pattern around a tube, which are the stagnation zone above the tube and the void zone below it [13]. These features exert a substantial influence on the heat transfer characteristics, resulting in a higher intensity in the upper part of the tube [14, 15]. Their influence factors mainly include granular properties (such as particle density, diameter, and geometric shape), particle velocities and temperatures, contact parameters, tube arrangements, vertical and horizontal tube spacings, operation conditions, etc. When it comes to heat transfer enhancement, a multitude of methodologies have been explored to mitigate the formation of stagnation zones and void zones, so that to reduce contact and penetration thermal resistances. The research group of Qiuwang Wang has made significant contributions to the geometry and layout optimization of heat exchange tubes in this field, for instance, changing the tube section shape [16], implementing additional tube oscillation [17], and tilting the tube to enhance heat transfer intensity [18]. In addition, other methods such as adding internals [12] have also been extensively explored. The literature surveyed above primarily comprises laboratory-scale experiments, theoretical calculations, and numerical simulations. Among these methods, numerical simulations provide a good perspective for further investigation and lead to its increasing utilization. To our knowledge, the numerical simulation approaches can be divided into two-fluid method (TFM), discrete element method (DEM), and the combined approach of Computational Fluid Dynamics with Discrete Element Method (CFD-DEM). Compared to the TFM and DEM, CFD-DEM can achieve the most realistic simulation and further provide a comprehensive understanding of gas-solid flow and the corresponding heat transfer characteristics [19–21]. Nevertheless, only a limited number of studies can be found that have investigated the tubular or typical MBHEs on the basis of CFD-DEM. Furthermore, to our knowledge, several studies have been conducted to assess the influence of operating conditions on overall heat transfer. The research conducted by Shen et al. [22] revealed that particle shape has a significant impact on heat transfer performance in MBHE by influencing the flow pattern of particles around the tube. Meanwhile, the influence of the temperature distribution within individual particles on the heat transfer intensity, as well as the released sensible and latent heat, was investigated by Feng et al. [23]. Moreover, Zhang et al. [24] have proved that the particle size distribution in a particle vertical moving bed can significantly affect the distributions of particle temperature and void fraction, further influencing the exergy recovery. The findings from researches by Qiu et al. [25], Yang et al. [26], and Morris et al. [27] demonstrated that inlet air mass flux, bed height, particle mass flow rate, particle inlet temperature, and tube geometric configuration all can affect heat transfer to a certain extent with different effects. However, insufficient attention has been given to the effects of operation conditions on heat transfer process in tubular MBHEs from a simulation perspective using CFD-DEM. Specifically, the effects of three operation parameters, widely acknowledged as fundamental and crucial with a significant degree of adjustment: particle inlet temperature, tube wall temperature, and particle descent velocity, have not received adequate consideration.

Given these research limitations, we introduce a robust and practical numerical approach based on CFD-DEM for the simulation of tubular MBHEs. This method incorporated four heat transfer sub-models are provided, including contact heat conduction, gas film heat conduction, heat radiation, and heat convection, besides, while also accounting for artificial softening correction. The method is further validated by experiments conducted in the high-temperature region, approximately around 600°C. Then, based on the experimental conditions, further investigations on the effects of operation conditions, including particle inlet particle temperature, tube wall temperature, and particle descent velocity, are conducted on the basis of the developed method. This study provides a simulation-based perspective using CFD-DEM to further explore the main influence factors of heat transfer in tubular MBHEs. The insights gleaned from this research can contribute to further advancements in the development of efficient tubular MBHEs.

2. Methodology

2.1 CFD-DEM approach

In this section, a brief introduction is provided on the CFD-DEM based approach, which primarily encompasses the continuous phase model, discrete phase model, and coupling method. The detailed descriptions can be found in our previous work [28].

Governing equations of gas phase mainly include continuity equation, momentum conservation equations, and energy conservation equations (see Ref. [29] for details), which are listed in Table 1 for convenience. The Gidaspow drag model is employed while Soave RK equations and default parameters are adopted to simulate the change in fluid density.

The discrete phase is described on the basis of DEM in this work. Each particle is tracked during the simulation,

whose motion is calculated based on the Newton's second law. Besides, Hertz-Mindlin (no slip) with Standard Rolling Friction model, one of the soft-sphere collision models, is adopted to character the contact forces and torques. In order to expedite the calculation, particle rotation is disregarded in practice. The detailed governing equations of discrete phase are listed in Table 2 (see Ref. [31] for details).

Table 1 Main governing equations of gas phase

Continuity equation [29]
$\frac{\partial}{\partial t}\left(\alpha_{\mathrm{f}}\rho_{\mathrm{f}}\right)+\nabla\cdot\left(\alpha_{\mathrm{f}}\rho_{\mathrm{f}}\boldsymbol{v}_{\mathrm{f}}\right)=0$
Momentum conservation equations [29]
$\frac{\partial}{\partial t}\left(\alpha_{\mathrm{f}}\rho_{\mathrm{f}}\boldsymbol{v}_{\mathrm{f}}\right)+\nabla\cdot\left(\alpha_{\mathrm{f}}\rho_{\mathrm{f}}\boldsymbol{v}_{\mathrm{f}}\boldsymbol{v}_{\mathrm{f}}\right)=-\alpha_{\mathrm{f}}\nabla p_{\mathrm{f}}+\alpha_{\mathrm{f}}\rho_{\mathrm{f}}\boldsymbol{g}+\nabla\cdot\bar{\bar{\tau}}_{\mathrm{f}}+\boldsymbol{F}_{\mathrm{pf}}$
$\bar{\bar{\tau}}_{\mathrm{f}}=\alpha_{\mathrm{f}}\mu_{\mathrm{f}}\left(\nabla\boldsymbol{v}_{\mathrm{f}}+\nabla\boldsymbol{v}_{\mathrm{f}}^{\mathrm{T}}\right)+\alpha_{\mathrm{f}}\left(b_{\mathrm{f}}-\frac{2}{3}\mu_{\mathrm{f}}\right)\nabla\cdot\boldsymbol{v}_{\mathrm{f}}\bar{\bar{I}}$
Gidaspow drag model [30]
$\boldsymbol{F}_{\mathrm{pf}}=K_{\mathrm{pf}}\left(\boldsymbol{v}_{\mathrm{p}}-\boldsymbol{v}_{\mathrm{f}}\right)$
$K_{\mathrm{pf}}=\begin{cases}150\frac{\left(1-\alpha_{\mathrm{f}}\right)^2\mu_{\mathrm{f}}}{\alpha_{\mathrm{f}}d_{\mathrm{p}}}+1.75\frac{\left(1-\alpha_{\mathrm{f}}\right)\rho_{\mathrm{f}}\left\lvert\boldsymbol{v}_{\mathrm{p}}-\boldsymbol{v}_{\mathrm{f}}\right\rvert}{d_{\mathrm{p}}} & ,\alpha_{\mathrm{f}}\le 0.8\\ 0.75C_{\mathrm{D}}\frac{\left(1-\alpha_{\mathrm{f}}\right)\alpha_{\mathrm{f}}\rho_{\mathrm{f}}\left\lvert\boldsymbol{v}_{\mathrm{p}}-\boldsymbol{v}_{\mathrm{f}}\right\rvert}{d_{\mathrm{p}}}\alpha_{\mathrm{f}}^{-2.65} & ,\alpha_{\mathrm{f}}>0.8\end{cases}$
$C_{\mathrm{D}}=\begin{cases}\frac{24}{\alpha_{\mathrm{f}}Re_{\mathrm{p}}}\left(1+0.15\alpha_{\mathrm{f}}Re_{\mathrm{p}}^{0.687}\right) & ,Re_{\mathrm{p}}\le 1000\\ 0.44 & ,Re_{\mathrm{p}}>1000\end{cases}$
$Re_{\mathrm{p}}=\frac{\rho_{\mathrm{f}}d_{\mathrm{p}}\left\lvert\boldsymbol{v}_{\mathrm{p}}-\boldsymbol{v}_{\mathrm{f}}\right\rvert}{\mu_{\mathrm{f}}}$
Energy conservation equations [29]
$\frac{\partial}{\partial t}\left(\alpha_{\mathrm{f}}\rho_{\mathrm{f}}E_{\mathrm{f}}\right)+\nabla\cdot\left(\alpha_{\mathrm{f}}\rho_{\mathrm{f}}\boldsymbol{v}_{\mathrm{f}}E_{\mathrm{f}}\right)$
$=\nabla\cdot\left(\alpha_{\mathrm{f}}k_{\mathrm{eff,f}}\nabla T_{\mathrm{f}}+\bar{\bar{\tau}}_{\mathrm{eff,f}}\cdot\boldsymbol{v}_{\mathrm{f}}\right)+p_{\mathrm{f}}\frac{\partial\alpha_{\mathrm{f}}}{\partial t}+Q_{\mathrm{pf}}+Q_{\mathrm{fw}}$
$\bar{\bar{\tau}}_{\mathrm{eff,f}}=\alpha_{\mathrm{f}}\mu_{\mathrm{eff,f}}\left(\nabla\boldsymbol{v}_{\mathrm{f}}+\nabla\boldsymbol{v}_{\mathrm{f}}^{\mathrm{T}}\right)+\alpha_{\mathrm{f}}\left(b_{\mathrm{eff,f}}-\frac{2}{3}\mu_{\mathrm{eff,f}}\right)+\nabla\cdot\boldsymbol{v}_{\mathrm{f}}\bar{\bar{I}}$
$\begin{cases}E_{\mathrm{f}}=h_{\mathrm{f}}-p_{\mathrm{f}}+p_{\mathrm{f,op}}/\rho_{\mathrm{f}}+\boldsymbol{v}_{\mathrm{f}}^2/2\\ k_{\mathrm{eff,f}}=k_{\mathrm{f,ref}}\sqrt{T_{\mathrm{f}}/T_{\mathrm{f,ref}}}\\ \mu_{\mathrm{eff,f}}=\mu_{\mathrm{f,ref}}\sqrt{T_{\mathrm{f}}/T_{\mathrm{f,ref}}}\\ b_{\mathrm{eff,f}}=b_{\mathrm{f,ref}}\sqrt{T_{\mathrm{f}}/T_{\mathrm{f,ref}}}\end{cases}$

The unresolved coupling method of CFD and DEM is adopted in this study, including the momentum coupling method and energy coupling method. The equations mentioned above are respectively solved separately in Ansys Fluent and EDEM. A direct coupling is used while the equations mentioned above are respectively solved separately in Ansys Fluent and EDEM. Data sharing occurs between the particle phase and the fluid phase. During the energy coupling process, this primarily involves temperature data and convective heat flux data. In the momentum coupling process, it includes particle and fluid velocities, along with gas-solid drag forces. A simulation step is deemed convergent when the continuity residual, momentum residual, and energy residual between consecutive iterations are each below 1.0×10^{-3}, 1.0×10^{-4}, and 1.0×10^{-6}, respectively. Besides, the additional heat transfer models in EDEM are incorporated through the application programming interface (API), while computational data interaction between Fluent and EDEM is by user-defined function (UDF).

Table 2 Main governing equations of discrete phase

Motion model [31]
$m_{\mathrm{p}}\frac{\mathrm{d}\boldsymbol{v}_{\mathrm{p}}}{\mathrm{d}t}=m_{\mathrm{p}}\boldsymbol{g}+\boldsymbol{F}_{\mathrm{c}}+\boldsymbol{F}_{\mathrm{fp}}$
$I_{\mathrm{p}}\frac{\mathrm{d}\boldsymbol{\omega}_{\mathrm{p}}}{\mathrm{d}t}=\boldsymbol{\tau}_{\mathrm{p}}$
Contact model [31]
$\boldsymbol{F}_{\mathrm{n}}=\boldsymbol{F}_{\mathrm{n}}^{\mathrm{s}}+\boldsymbol{F}_{\mathrm{n}}^{\mathrm{d}}$
$\boldsymbol{F}_{n}^{s}=\frac{4}{3}E^{*}\left(R^{*}\right)^{\frac{1}{2}}\alpha^{\frac{3}{2}}$
$\boldsymbol{F}_{\mathrm{n}}^{\mathrm{d}}=-2\sqrt{\frac{5}{6}}\beta\sqrt{S_{\mathrm{n}}m^{*}}\boldsymbol{v}_{\mathrm{n}}^{\mathrm{rel}}$
$\boldsymbol{F}_{\mathrm{t}}=\min\left\{\mu_{\mathrm{s}}\boldsymbol{F}_{\mathrm{n}},\boldsymbol{F}_{\mathrm{t}}^{\mathrm{s}}+\boldsymbol{F}_{\mathrm{t}}^{\mathrm{d}}\right\}$
$\boldsymbol{F}_{\mathrm{t}}^{\mathrm{s}}=-S_{\mathrm{t}}\delta$
$\boldsymbol{F}_{\mathrm{t}}^{\mathrm{d}}=-2\sqrt{\frac{5}{6}}\beta\sqrt{S_{\mathrm{t}}m^{*}}\boldsymbol{v}_{\mathrm{t}}^{\mathrm{rel}}$
$\boldsymbol{\tau}=-\mu_{\mathrm{r}}R\boldsymbol{F}_{\mathrm{n}}\boldsymbol{\omega}$
$\begin{cases}E^{*}=\left(1-v_1^2\right)/E_1+\left(1-v_2^2\right)/E_2\\ \beta=-\ln e/\sqrt{\ln^2 e+\pi^2}\\ m^{*}=m_1m_2/\left(m_1+m_2\right)\\ S_{\mathrm{n}}=2E^{*}\sqrt{R^{*}\alpha}\\ G^{*}=\left(2-v_1^2\right)/G_1+\left(2-v_2^2\right)/G_2\end{cases}$

2.2 Heat transfer sub-models

For tubular MBHEs, heat transfer occurs through various mechanisms including particle-to-particle (P-P)/particle-to-wall (P-W) contact heat conduction, P-P/P-W heat conduction through interstitial fluid, P-P/P-W heat radiation, fluid-to-particle (F-P)/fluid-to-wall (F-W) heat convection, as well as F-P/F-W heat radiation. Besides, heat radiation involved with the fluid is neglected, as the interstitial air can be considered a transparent medium. Meanwhile, the conversion of kinetic energy into heat energy caused by collisions and friction between particles, as well as between particles and walls, is also ignored due to the observation that particle velocities are relatively small (~mm/s), especially in densely packed conditions, indicating lower kinetic energy of the particles. The details of the heat transfer sub-models are listed in Table 3 (see Ref. [28] for details).

2.3 Simulation settings

The model assumptions are quite similar with our another research [28]. Herein, the model ignores conduction heat resistances in tube walls, assumes laminar flow for the air, considers air radiation as negligible, treats all walls except the tube wall as adiabatic, and maintains the tube wall temperature at a constant level. The detailed discussions can be found in the original literature.

As shown in Fig. S1, this work continues to utilize the single-tube MBHE and its grids established in our previous study [28], including CFD body-fitted grids with its number of 656 (marked with a black box) and DEM orthogonal grids with its number of 420. Due to the nature of unresolved CFD-DEM, the mesh size to particle diameter ratio has been set to approximately 3.1 for the CFD grids, a value within the recommended range (between 3.0 and 10.0) [33]. Besides, several key parameters used in CFD-DEM simulations remain consistent with those in our previous work [28] and are listed in Table S1, consisting of physical property parameters, contact parameters, and calculation parameters.

Table 3 Heat transfer sub-models [28]

<table>
<tr><td>Contact heat conduction model</td><td>Heat convection model</td></tr>
<tr><td>$$h_{\mathrm{cc}}=\frac{4k_1k_2}{k_1+k_2}\left(\frac{3\left|\boldsymbol{F}_{\mathrm{n}}\right|R^*}{4E^*}\right)^{1/3},\quad Q_{\mathrm{cc}}=h_{\mathrm{cc}}\Delta T$$</td><td>$$Q_{\mathrm{fp}}=h_{\mathrm{c,fp}}A_i\left(T_{\mathrm{p}}-T_{\mathrm{f}}\right),\quad h_{\mathrm{c,fp}}=\frac{\lambda_{\mathrm{f}}Nu_{\mathrm{p}}}{l_{\mathrm{p}}}$$
$$Nu_{\mathrm{p,Gunn}}=\left(7-10\alpha_{\mathrm{f}}+5\alpha_{\mathrm{f}}^2\right)\left(1+0.7Re_{\mathrm{p}}^{0.2}Pr^{1/3}\right)+\left(1.33-2.4\alpha_{\mathrm{f}}+1.2\alpha_{\mathrm{f}}^2\right)Re_{\mathrm{p}}^{0.7}Pr^{1/3}$$
$$0<Re_{\mathrm{p}}<10^5,\ 0.35<\alpha_f<1$$
$$Pr=\frac{C_{\mathrm{pf}}\mu_{\mathrm{f}}}{k_{\mathrm{f}}}$$
$$Q_{\mathrm{fw}}=\lambda_{\mathrm{f}}\left(\frac{\partial T}{\partial n}\right)_{\mathrm{wall}}$$</td></tr>
<tr><td>Gas film heat conduction model</td><td>Artificial softening correction method</td></tr>
<tr><td>$$Q_{\mathrm{gfc}}=h_{\mathrm{gfc}}\Delta T$$
$$h_{\mathrm{gfc}}=\begin{cases}\lambda_{\mathrm{f}}\int_{\beta_2}^{\alpha_1}\frac{2\pi R\sin\theta\mathrm{d}\left(R\sin\theta\right)}{l_{ij}-2R\cos\theta},l_{ij}<d_{\mathrm{p}}+\delta\ \ (\mathrm{P\text{-}P})\\ \lambda_{\mathrm{f}}\int_{\beta_2}^{\alpha_2}\frac{2\pi R\sin\theta\mathrm{d}\left(R\sin\theta\right)}{l_{ij}-R\cos\theta},l_{ij}<R+\delta\ \ (\mathrm{P\text{-}W})\end{cases}$$
$$\begin{cases}\alpha_1=\arccos\left[\frac{l_{ij}^2+R^2-\left(R+\delta\right)^2}{2l_{ij}R}\right]\\ \beta_1=\begin{cases}0,d_{\mathrm{p}}+2\eta_{\mathrm{p}}\le l_{ij}<d_{\mathrm{p}}+\delta\\ \arccos\left(\frac{l_{ij}-2\eta_p}{d_{\mathrm{p}}}\right),l_{ij}<d_{\mathrm{p}}+2\eta_{\mathrm{p}}\end{cases}\end{cases}$$
$$\begin{cases}\alpha_2=\arccos\left(\frac{l_{ij}}{R+\delta}\right)\\ \beta_2=\begin{cases}0,R+\eta_{\mathrm{p}}+\eta_{\mathrm{w}}\le l_{ij}<R+\delta\\ \arccos\left(\frac{l_{ij}-\eta_{\mathrm{p}}-\eta_{\mathrm{w}}}{R}\right),l_{ij}<R+\eta_{\mathrm{p}}+\eta_{\mathrm{w}}\end{cases}\end{cases}$$</td><td>$$F_{\mathrm{pp}}=\left(\frac{E_{\mathrm{simu}}}{E_{\mathrm{real}}}\right)^{\frac{1}{5}},F_{\mathrm{pw}}=\left(\frac{\frac{1-\nu_1^2}{E_{1,\mathrm{real}}}+\frac{1-\nu_2^2}{E_{2,\mathrm{real}}}}{\frac{1-\nu_1^2}{E_{1,\mathrm{simu}}}+\frac{1-\nu_2^2}{E_{2,\mathrm{simu}}}}\right)^{\frac{1}{5}}$$
$$Q_{\mathrm{cc}}=\begin{cases}F_{\mathrm{pp}}\frac{4k_1k_2}{k_1+k_2}\left(\frac{3\left|\boldsymbol{F}_n\right|R^*}{4E^*}\right)^{1/3}\Delta T,\ \mathrm{P\text{-}P}\\ F_{\mathrm{pw}}\frac{4k_1k_2}{k_1+k_2}\left(\frac{3\left|\boldsymbol{F}_n\right|R^*}{4E^*}\right)^{1/3}\Delta T,\ \mathrm{P\text{-}P}\end{cases}$$
$$l_{ij}^{\mathrm{real}}=\begin{cases}2\sqrt{R^2-F_{\mathrm{pp}}^2\left[R^2-\left(\frac{l_{ij}^{\mathrm{simu}}}{2}\right)^2\right]},\ \mathrm{P\text{-}P}\\ \sqrt{R^2-F_{\mathrm{pw}}^2\left(R^2-l_{ij}^{\mathrm{simu2}}\right)},\ \mathrm{P\text{-}W}\end{cases},$$
when i and j are in contact</td></tr>
<tr><td>Heat radiation model</td><td>Temperature update model</td></tr>
<tr><td>$$\begin{cases}Q_{\mathrm{rad}}^{\mathrm{p\text{-}p}}=\frac{\sigma\left(T_{\mathrm{p1}}^4-T_{\mathrm{p2}}^4\right)}{\frac{1-\varepsilon_{\mathrm{p1}}}{\varepsilon_{\mathrm{p1}}}\frac{1}{A_1F_{12}^{\mathrm{p\text{-}p}}}+\frac{1}{A_1F_{12}^{\mathrm{p\text{-}p}}}+\frac{1-\varepsilon_{\mathrm{p2}}}{\varepsilon_{\mathrm{p2}}}\frac{1}{A_2F_{21}^{\mathrm{p\text{-}p}}}},A_1F_{12}^{\mathrm{p\text{-}p}}=A_2F_{21}^{\mathrm{p\text{-}p}},A_1=4\pi R^2\\ Q_{\mathrm{rad}}^{\mathrm{p\text{-}w}}=\frac{\sigma\left(T_p^4-T_{\mathrm{w}}^4\right)}{\frac{1-\varepsilon_{\mathrm{p}}}{\varepsilon_{\mathrm{p}}}\frac{1}{A_1F_{12}^{\mathrm{p\text{-}w}}}+\frac{1}{A_1F_{12}^{\mathrm{p\text{-}w}}}+\frac{1-\varepsilon_{\mathrm{w}}}{\varepsilon_{\mathrm{w}}}\frac{1}{A_2F_{21}^{\mathrm{p\text{-}w}}}},A_1F_{12}^{\mathrm{p\text{-}w}}=A_2F_{21}^{\mathrm{p\text{-}w}},A_1=4\pi R^2\end{cases}$$
The $F_{12}^{\mathrm{p\text{-}p}}$ and $F_{12}^{\mathrm{p\text{-}w}}$ can be calculated according to Refs. [28,32].</td><td>$$m_{\mathrm{p}}C_{\mathrm{pp}}\frac{\mathrm{d}T_{\mathrm{p}}}{\mathrm{d}t}=\sum Q_{\mathrm{px}}$$</td></tr>
</table>

2.4 Simulation cases and boundary conditions

The simulation cases are listed in Table 4. The reliability of the model has been verified for temperatures below 300°C [28]. However, its performance in high-temperature ranges remains uncertain. Therefore, in this study, an additional case (Case 1) has been introduced to assess the model's applicability at the temperature around 600°C. The inlet particle temperature (600°C) and tube wall temperature (40°C) are estimated based on the experimental conditions, and rounded to the nearest integer values. This study continues to utilize the experimental setup and procedures introduced in our previous research [28]. To maintain simplicity, it avoids reintroducing complex experimental details herein. Detailed verification of the simulation and experiment are discussed in Section 3.1. Thus, a semi-quantitative verification of the model can be obtained by comparing the simulation results of Case 1 with the corresponding experimental results. Case 2 is a base case while cases 3–17 are used to explore the effects of operation conditions on heat transfer in the single-tube MBHE, including inlet particle temperature, tube wall temperature, and particle descent velocity. Moreover, Case 18 is a supplementary for determining the optimize selection range of particle descent velocity. It is worth noting that the parameter varying ranges in our study were determined based on those used in our experiments and practical engineering applications.

Table 4 Simulation cases and corresponding boundary conditions

Case	Inlet particle temperature/°C
1	600.0
2	600.0
3–6	500.0/550.0/650.0/700.0
7–10	600.0
11–17	600.0
18	600.0
Case	**Tube wall temperature/°C**
1	40.0
2	50.0
3–6	50.0
7–10	100.0/150.0/200.0/250.0
11–17	50.0
18	50.0
Case	**Particle descent velocity/mm·s^{-1}**
1	1.3
2	2.0
3–6	2.0
7–10	2.0
11–17	0.5/1.0/4.0/6.0/8.0/10.0/12.0
18	1.3

3. Results and Discussion

Treated as the focus of investigation, the tube wall simultaneously receives heat fluxes of contact heat conduction (HF_1), heat radiation (HF_2, actually including short-range and long-range components), gas film heat conduction (HF_3), and heat convection (HF_4). In other words, total heat flux of tube wall in simulation can be calculated by the equation $Q_{\mathrm{w}}^{\mathrm{simu}} = \sum_{i=1}^{4} \mathrm{HF}_i$. In order to effectively enhance heat transfer in tubular MBHEs, it is essential to understand the individual contributions of various heat transfer mechanisms to both the heat fluxes of the particles and the tube wall. Therefore, additional attention should be given to addressing these contributions and examining how they are influenced by operation parameters.

3.1 Additional experimental validation

Before extracting results for validation and further analysis, it is imperative for a simulation case to attain a quasi-stable state, characterized by minor fluctuations in heat and mass transfer results. Take Case 2 as an example, it can be observed from Fig. 1 that the related parameters, including $Q_{\mathrm{w}}^{\mathrm{simu}}$, particle descent velocity at the outlet, particle average temperature around the tube, fluid average temperature in the simulation domain, and particle number around the tube, gradually approach a state of near stability, after a coupling calculation time of 33 s. Meanwhile, the results depicted in Fig. 1 suggest that the particle average temperature around the tube primarily restricts the required simulation time to achieve a quasi-steady state. In this study, only the simulation results in quasi-stable state are adopted in order to ensure the result reliability. Generally, the sample space comprises the results obtained during the last 30 s under quasi-stable conditions, which is also shown in Fig. 1. Besides, in order to align the simulation conditions with the corresponding experimental conditions, the particle temperatures of Case 1 are fixed to the average values obtained from experiments, while those of other cases vary with simulation time.

For validation, the effective heat transfer coefficient, a key parameter for characterize the heat transfer intensity, is employed as a quantitative measure. In Case 1, the effective heat transfer coefficient in the simulation is 55.29 W/(m^2·K) while that in the experiment is

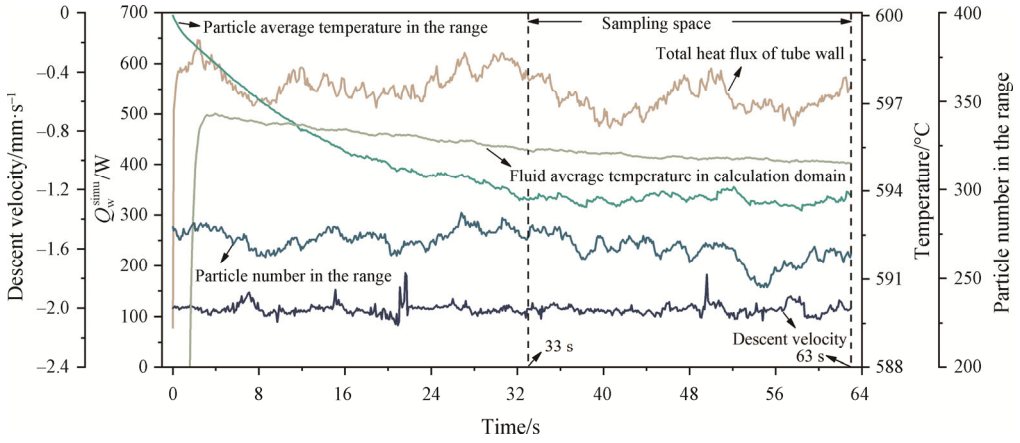

Fig. 1 The variation trends of several specific parameters with simulation time in the simulation of Case 2. The term "range" here denotes the distance of $2d_p$ from a tube wall

60.43 W/(m^2·K), leading to a relative error of 8.5%. In comparison to the relative errors observed in previous low-temperature cases, which are 4.95%, 3.44%, and 4.58% respectively, the relative error of Case 1 is slightly higher due to the omissions of the relationship between some simulation parameters and temperature, such as particle Young's modulus. However, overall, the relative error of the high-temperature case is also within an acceptable range. Therefore, it can be concluded that the CFD-DEM model utilized in this study is relatively reliable.

3.2 Effect of inlet particle temperature

Herein, the inlet particle temperature, which is regarded as a potential factor affecting heat transfer, is assumed to be uniformly distributed and fixed at a given value, without taking into account the possible temperature distribution of feeding particles in spatial-temporal scale (to simplify the study). Given this, it can be predicted that the heat exchange between hot particles and cool tube wall will be greatly enhanced with the increase of inlet particle temperature because the heat transfer temperature difference expands at the same time.

As shown in Fig. 2, consistent with the prediction, the value of Q_w^{simu} (HF_{total}) significantly increases from 394.9 W to 713.0 W with the inlet particle temperature rising from 500°C to 700°C. It can also be observed from Fig. 2 that all the components of HF_{total} exhibit different increasing trends with respect to the inlet particle temperature. The results suggest that HF_2 has the greatest rise as the temperature increases, even exceeding HF_3 at temperatures greater than 650°C. This phenomenon can be attributed to the inherent high-order relationship between heat radiation and particle temperature. This relationship leads to a significant sensitivity of HF_2 to particle temperature, particularly within a relatively high-temperature range (>650°C).

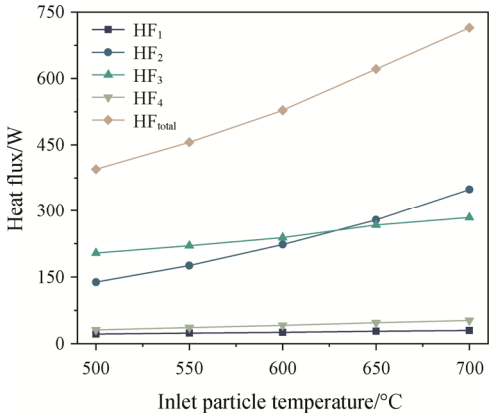

Fig. 2 The relationships between various heat fluxes and the inlet particle temperature

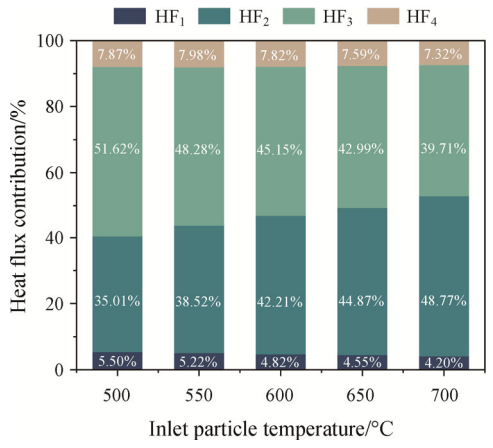

Fig. 3 Heat flux contributions of different heat transfer mechanisms vary with inlet particle temperatures

From Fig. 3, it can be seen that, among all the components of HF_{total}, HF_2 (42.21% at 600°C) and HF_3 (45.15% at 600°C) have contributed the most to the heat flux of tube wall, while HF_1 and HF_4 take up 7.82% and

4.82% at 600°C, respectively. It should be noticed that in our previous investigation [28], the contribution of HF_2 is higher than 60% as the temperature is lower than 300°C. This observation indicates that, within the studied conditions, heat radiation and gas film heat conduction play dominant roles in the heat transfer process, which is consistent with the results of Xiao et al. [34]. This can serve as a stepping stone for further improvements in the heat transfer efficiency of tubular MBHEs. Similarly, these contributions are significantly affected by the inlet particle temperature. It can also be noticed from Fig. 3 that with the increase of inlet particle temperature, the proportion of heat radiation significantly increases and gradually surpasses that of gas film heat conduction, contact heat conduction, and heat convection as inlet particle temperature increases. Given this, it can be inferred that the heat transfer mode of the particle-fluid-wall system within tubular MBHEs gradually transitions from being dominated by gas film heat conduction to being dominated by heat radiation.

Overall, the higher temperature can result in higher heat transfer intensity. However, in practice, the inlet particle temperature tends to be a given value, which depends on what material is the particle made of or what process is the particle obtained from. For example, the inlet temperature of hot coke usually is greater than 700°C in coke dry quenching bed [35], while that of common hot pellets in tubular MBHE ranges from 100°C to 800°C [36]. This fact also gives us an enlightenment that minimizing heat loss prior to the granular materials entering the heat exchanger is crucial in order to maintain a higher temperature level of the particles.

3.3 Effect of tube wall temperature

The tube wall temperature defined in this study refers to the average temperature of tube outer wall (in direct contact with particles). According to engineering experience, the temperature field on the surface of a certain heat exchange tube is not uniform in the most cases, with lower temperature near the inlet and higher temperature near the outlet. This nonuniform distribution of tube wall temperature is mainly caused by the uneven temperature distributions of particle and working medium along the tube. Given this, in actual engineering, with the flow rate of the working medium, its thermal state, and particle temperature distribution varying, the tube wall temperature potentially becomes a variable operation parameter. Actually, when further taking the working medium side simulation into account, the tube wall temperature is a solvable variable. However, simulating systems that involve particles, air, water, and walls is challenging due to the complexity of fluid-structure coupling. Therefore, in this work, the tube wall temperature is considered as a variable operational parameter to directly investigate its effect on heat transfer, assuming a simplified uniform temperature distribution pattern.

The results presented in Fig. 4 suggest that HF_{total} exhibits a downward trend with the rise of tube wall temperature while its components other than HF_2 show a decrease trend. Among the components of HF_{total}, HF_3 has the biggest reduction with tube wall temperature increasing from 50°C to 250°C, while HF_2 presents no obvious pattern. This result suggests that the P-W gas film heat conduction is much more sensitive to the variation of tube wall temperature and P-W heat radiation exhibits less sensitive. This may be attributed to that, within the studied range of tube wall temperature, more influence has been exerted on HF_3, despite its first-order relation with temperature. In other words, the discrepancy of the sensitive ranges for P-W heat radiation and P-W gas film heat conduction to tube wall temperature leads to this controversial behavior. Similar to other cases, HF_2 and HF_3 are still dominant at different tube wall temperatures, and together they account for about 90% of HF_{total}, which is shown in Fig. 5. Furthermore, as the tube wall temperature increases, there is a tendency for the heat transfer mode to shift towards a radiation-dominated mode. This can be attributed to the fact that the contribution of P-W heat radiation increases from 42.21% to 51.36% when the tube wall temperature rises from 50°C to 250°C. Moreover, the affecting mechanism of tube wall temperature on heat transfer is quite similar to that of inlet particle temperature, which is mainly embodied at influencing the heat transfer temperature difference.

In conclusion, the increase of tube wall temperature is not conducive to heat transfer enhancement. The tube wall temperature can be regarded as the result of heat transfer in particle-fluid-wall system, which depends on the temperature and descent velocity of surrounding particles, working medium parameters, fluid mass flow rate, as well as other factors influencing the heat transfer process. Assuming that the heat transfer process reaches a quasi-steady state with a thin tube wall and a material of high thermal conductivity is used, the local tube wall temperature can be considered as the working medium temperature at the corresponding location. From this point of view, to mitigate the impact of high tube wall temperature on heat transfer efficiency, several measures can be taken. These include, but are not limited to, increasing the flow rate of the working fluid, improving the specific heat capacity of the working medium, and optimizing the arrangement of the heat transfer path to obtain high temperature difference. However, these methods aimed at reducing the tube wall temperature may have multiple associated effects. For example, increasing the flow rate of the working medium can lead

to a lower temperature rise of the fluid flowing through the tube, which can further result in degraded product quality or increased demand for heat exchange area. To increase the heat exchange area, enlarging tube diameter or adding more tubes is feasible. However, it's not yet clear whether these measures inhibit or promote heat transfer in our cases, which requires further study. Therefore, to evaluate the comprehensive effects of these methods on overall heat transfer, it is necessary to figure out all the potential effects through targeted experiments and simulations.

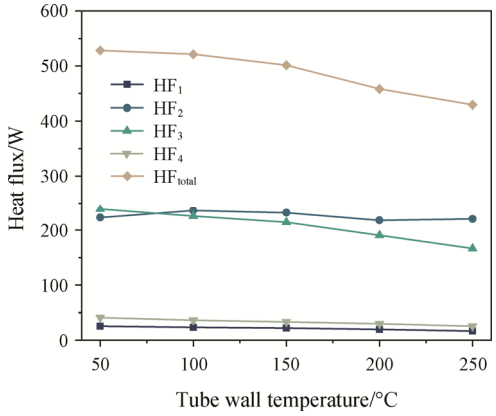

Fig. 4 The relationships between various heat fluxes and the tube wall temperature

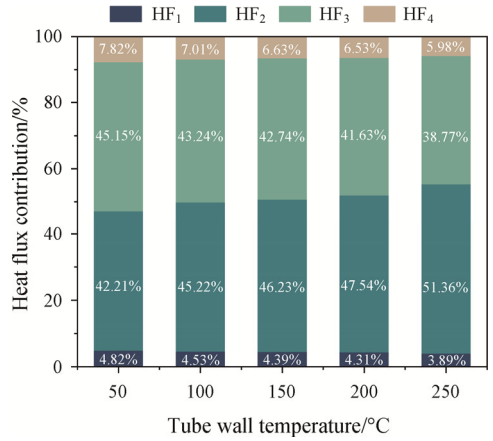

Fig. 5 Heat flux contributions of different heat transfer mechanisms vary with tube wall temperatures

3.4 Effect of particle descent velocity

Particle descent velocity, a flexible and adjustable operation parameter, is another essential factor for affecting heat transfer. The evolutions of Q_w^{simu} with the increase of descent velocity are illustrated in Fig. 6. Q_w^{simu} presents an unexpected trend as the descent velocity rises from 0.5 mm/s to 12 mm/s. The tendency can be divided into three stages: (1) the ascent stage when the velocity is relatively small; (2) the descent stage when the velocity is moderate; and (3) the stable stage when the velocity is relatively high. As for the components of Q_w^{simu}, the heat transfer contributions of HF_s (s=1–4) follow the order from strong to weak: HF_3 (45.02%–46.37%), HF_2 (40.63%–43.38%), HF_4 (6.07–9.41%), and HF_1 (4.58%–4.84%), as illustrated in Fig. 7 and Fig. 8.

In Fig. 7, the proportions of HF_1 and HF_3 remain relatively unchanged to some extent while the proportion of HF_4 increases as that of HF_2 proportion decreases. This reveals that the descent velocity exerts a positive effect on HF_4. This effect can be attributed to the enhanced fluid flow in the system resulting from a stronger gas-solid drag force at greater particle velocities, which in turn leads to an enhanced F-W heat convection. However, even in this scenario, it can still be considered that the particle descent velocity exerts little effect on the

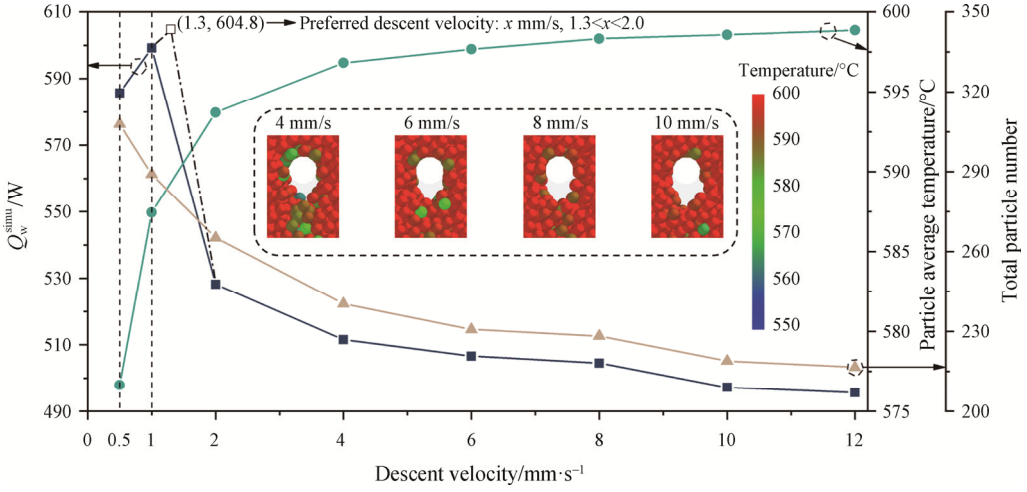

Fig. 6 The evolutions of Q_w^{simu} as well as average temperature and total number of particles around the tube ([d_p/2,2d_p]), with the increase of descent velocity

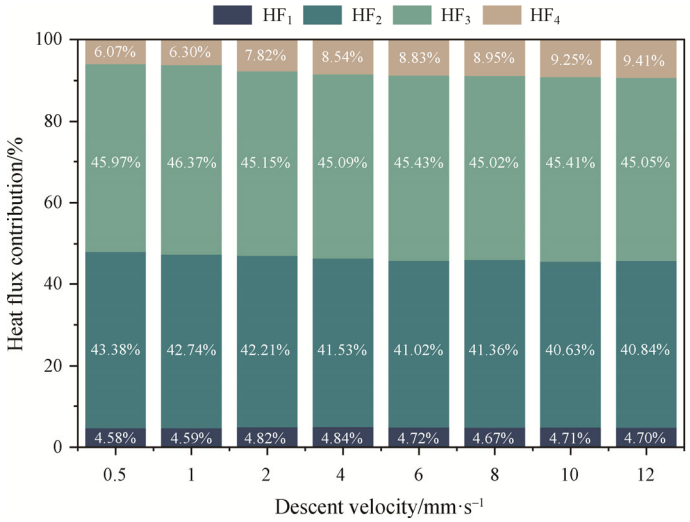

Fig. 7 Heat flux contributions of different heat transfer mechanisms vary with tube wall temperatures

change of heat transfer mode dominated by heat radiation and gas film conduction. This finding is consistent with that of our previous work [28]. The results in Fig. 8 reveal the trends of HF_s (s=1–3) and Q_w^{simu} with the descent velocity show a certain of similarity. However, the upward trend of HF_4 is also present. This suggests the tendency of Q_w^{simu} is mainly caused by HF_s (s=1–3). To shed light on this matter, Fig. 6 further depicts the corresponding evolutions of the average temperature and total number of particles surrounding the tube with the rise of particle descent velocity. The results show that, as the particle descent velocity increases, the particle average temperature steadily increases while the total particle number exhibits a totally opposite tendency. The level of particle average temperature reflects the temperature difference of heat transfer, in other words, the thickness of temperature boundary layer [34, 37]. In general, the greater the particle descent velocity, the shorter the thermal contact time or heat transfer time of particles [37], leading to the increase of particle temperature. Similar to fluid flow, this phenomenon leads to the thinning of the temperature boundary layer in the granular bulk, which in turn contributes to an enhanced heat transfer. Nevertheless, unlike fluids, the discontinuity of granular materials, especially for particles with large diameter, will lead to a unique flow pattern, that is, a slowdown zone above the tube along with a cavity region below the tube [13, 38], as presented in the illustration in Fig. 6 and Fig. 9. The slowdown zone refers to a region where the velocities of particles are relatively small compared to those of the main stream particles. In other words, particles within this zone experience a deceleration in their movement, which is caused by the strong P-P and P-W interaction. The results show that an increase in particle descent velocity can lead

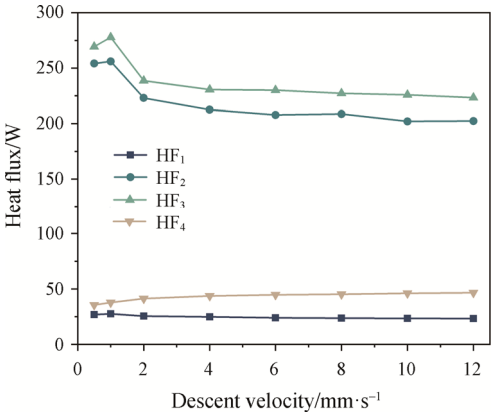

Fig. 8 The relationships between various heat fluxes and the particle descent velocity

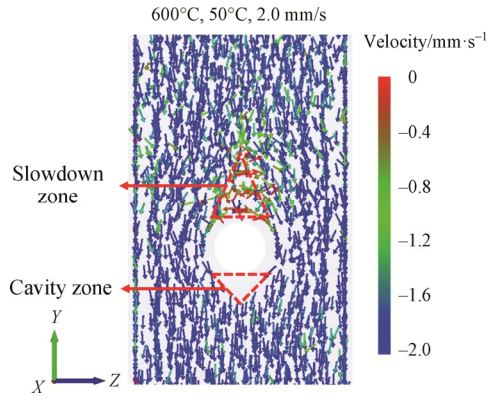

Fig. 9 The typical particle velocity vector diagram with the conditions of Case 2

to an expansion of the so-called cavity region, which further causing the granular bulk to become more and more loose. This is directly reflected in the sharp decrease of the total particle number within the studied

range, from 308 to 216, which is an adverse factor for heat transfer enhancement. Therefore, the unique evolution trend of Q_w^{simu} can be attributed to the competition of two main factors, temperature boundary layer thinning and cavity region volume increasing, as increasing particle descent velocity.

Moreover, from the evolution of Q_w^{simu}, on the one hand, there should exist an optimal value for the particle descent velocity, at which the heat transfer intensity can be maximized (here refers to preferred descent velocity x). On the other hand, the results suggest that: (1) when the descent velocity is relatively small (<x mm/s), the enhancement of P-W heat transfer is mainly influenced by the temperature boundary layer around the tube; (2) with descent velocity rising from x mm/s to 4 mm/s, the restriction of the cavity region volume increasing is gradually intensified and exceed the favor effect of temperature boundary layer thinning, leading to a sharp drop in heat transfer capacity; and (3) as the velocity continues to increase from 4 mm/s, both of the opposing impacts gradually diminish, further leading to the formation of a stable stage. Furthermore, it is crucial to figure out the exact value of x for engineering application. At this velocity, the two opposite effects can reach a balance with each other. However, due to the limitation of computing resources, it takes a long time to calculate the conditions with relatively low descent velocity. The results reveal that preferred descent velocity should be in the range from 1.3 mm/s to 2 mm/s, as illustrated in Fig. 6. However, the specific value of the preferred descent velocity is conditional, and it may depend on the operation conditions, the device configurations, and other parameters. Moreover, numerous studies have demonstrated that the impact of solid particles on other particles or walls can cause erosion or abrasion between them to varying degrees, posing challenges to the stable and safe operation of the system [5, 14, 39]. From engineering experience, it can be anticipated that the increase of particle descent velocity can lead to increased P-P and P-W wears to some extent. Therefore, for practice application, the descent velocity should be decided carefully from the two perspectives, which are the heat transfer aspect as well as equipment wear aspect. From this perspective, the local optimum heat transfer condition of the particle-fluid-wall system can be obtained within a suitable range of descent velocity, provided that the criterion for abrasion loss is met. Furthermore, while numerical simulations can offer valuable insights, it is also recommended to complement them with relevant experiments in order to determine the operational conditions that meet practical requirements. By combining both approaches, a more comprehensive understanding can be gained, ensuring that the desired effects are achieved efficiently.

4. Conclusions

This work introduces a viable and practical CFD-DEM approach with a certain level of simulation accuracy in both low and high-temperature ranges. Based on this, the effects of operation parameters, including inlet particle temperature, tube wall temperature, and particle descent velocity, on heat transfer in tubular MBHE are investigated in detail. The main conclusions are listed as follows:

(1) The overall heat transfer intensity as well as all forms of heat exchange can be enhanced by increasing inlet particle temperature from 500°C to 700°C, due to the positive effect of increasing inlet particle temperature on the increase of heat transfer temperature difference. Moreover, the tube wall temperature follows a similar mechanism. Consequently, an elevated tube wall temperature results in a reduction of heat transfer intensity. As the particle inlet temperature or tube wall temperature increases, there is a gradual shift in the heat transfer mode of the particle-fluid-wall system in tubular MBHEs. Specifically, the mode has an underlying trend to transition from being dominated by gas film heat conduction to a radiation-dominated mode.

(2) For particle descent velocity, there are significant differences in its influence on heat transfer in different ranges, which can be divided into ascent stage (0–x mm/s), descent stage (x–4.0 mm/s), and stable stage (>4.0 mm/s). Herein, x refers to the preferred descent velocity within the range from 1.3 mm/s to 2.0 mm/s. However, the particle descent velocity has little effect on the transition of heat transfer mode.

(3) From an optimization perspective, with the aim of improving heat transfer, it is recommended to implement proper thermal insulation on the inlet particles for maintaining a high temperature level throughout the granular bulk. Besides, to ensure an appropriate tube wall temperature, some importance should be attached to several factors such as the flow rate of the working fluid, modification of the working medium, and arrangement of the heat exchange tubes. Additionally, the simulation attempts suggest that a locally optimal descent velocity x is between 1.3 mm/s and 2.0 mm/s, with the highest heat transfer intensity. However, further analysis show that it is recommended to consider both heat transfer intensity and abrasion loss in the particle-fluid-wall system simultaneously when determining the actual descent velocity through experiments and simulations.

In conclusion, this study has elucidated the effects of three crucial operational parameters on overall heat transfer in a single-tube MBHE from a simulation-based perspective employing CFD-DEM. These findings have the potential to offer valuable insights for engineering applications and further advance the development of efficient tubular MBHEs.

Acknowledgments

This work is supported by the National Natural Science Foundation of China (No. 52276124). The authors gratefully acknowledge the guidance and support of Prof. Junfu LYU from the Department of Energy and Power Engineering at Tsinghua University.

Conflict of Interest

On behalf of all authors, the corresponding author states that there is no conflict of interest.

Electronic Supplementary Materials

Supplementary materials are available in the online version of this article at

https://doi.org/10.1007/s11630-024-2063-4

References

[1] Chen J., Zhou J., Li X., Huai X., Study of the heat transfer characteristics and waste heat recovery of hot gas with coagulative particles flowing through a moving granular bed filter (MGBF). Applied Thermal Engineering, 2022, 211: 118444.

[2] Liu J., Yu Q., Peng J., Hu X., Duan W., Thermal energy recovery from high-temperature blast furnace slag particles. International Communications in Heat and Mass Transfer, 2015, 69: 23–28.

[3] Feng J., Dong H., Liu J., Liang K., Gao J., Experimental study of gas flow characteristics in vertical tank for sinter waste heat recovery. Applied Thermal Engineering, 2015, 91: 73–79.

[4] Liu J., Liu Y., Liu C., Xin L., Yu W., Experimental and theoretical study on thermal stability of mixture R1234ze(E)/R32 in organic Rankine cycle. Journal of Thermal Science, 2023, 32: 1595–1613.

[5] Cheng Z., Tan Z., Guo Z., Yang J., Wang Q., Technologies and fundamentals of waste heat recovery from high-temperature solid granular materials. Applied Thermal Engineering, 2020, 179: 115703.

[6] Wen Z., Shi H.Z., Zhang X., Lou G.F., Liu X.L., Dou R.F., Su F.Y., Numerical simulation and parameters optimization on gas-solid heat transfer process of high temperature sinter. Ironmaking and Steelmaking, 2011, 38: 525–529.

[7] Leong J., Jin K., Shiau J., Jeng T., Tai C., Effect of sinter layer porosity distribution on flow and temperature fields in a sinter cooler. International Journal of Minerals, Metallurgy and Materials, 2009, 16: 265–272.

[8] Feng J.X., Liang K.L., Sun Z.B., Xu J.H., Zhang Y.M., Yang J.B., Cooling process of iron ore pellets in an annular cooler. International Journal of Minerals, Metallurgy and Materials, 2011, 18: 285–291.

[9] Albrecht K.J., Ho C.K., Design and operating considerations for a shell-and-plate, moving packed-bed, particle-to-sCO_2 heat exchanger. Solar Energy, 2019, 178: 331–340.

[10] Tian X., Yang J., Guo Z., Wang Q., Sunden B., Numerical study of heat transfer in gravity-driven dense particle flow around a hexagonal tube. Powder Technology, 2020, 367: 285–295.

[11] Qi C., Zhang Z., Wang M., Li Y., Gong X., Sun P., Zheng B., Effects of the structure parameters of horizontal tube bundles on particle flow performance in the heat exchanger. Case Studies in Thermal Engineering, 2023, 47: 103053.

[12] Jiang B., Xiang D., Zhang H., Pei H., Liu X., Effective waste heat recovery from industrial high-temperature granules: a moving bed indirect heat exchanger with embedded agitation. Energy, 2020, 208: 118346.

[13] Hertel J.D., Zunft S., Experimental validation of a continuum model for local heat transfer in shell-and-tube moving-bed heat exchangers. Applied Thermal Engineering, 2022, 206: 118092

[14] Guo Z., Tian X., Tan Z., Yang J., Wang Q., Optimization of gravity-driven granular flow around the tube for heat transfer enhancement. Chemical Engineering Transactions, 2019, 76: 247–252.

[15] Guo Z., Tian X., Wu Z., Yang J., Wang Q., Heat transfer of granular flow around aligned tube bank in moving bed: Experimental study and theoretical prediction by thermal resistance model. Energy Conversion and Management, 2022, 257: 115435.

[16] Tian X., Guo Z., Jia H., Yang J., Wang Q., Numerical investigation of a new type tube for shell-and-tube moving packed bed heat exchanger. Powder Technology 2021, 394: 584–596.

[17] Guo Z., Zhang S., Tian X., Yang J., Wang Q., Numerical investigation of tube oscillation in gravity-driven granular flow with heat transfer by discrete element method. Energy, 2020, 207: 118203.

[18] Guo Z., Yang J., Tan Z., Tian X., Wang Q., Numerical study on gravity-driven granular flow around tube out-wall: Effect of tube inclination on the heat transfer. International Journal of Heat and Mass Transfer, 2021, 174: 121296.

[19] Miao Z., Zhou Z., Yu A.B., Shen Y., CFD-DEM simulation of raceway formation in an ironmaking blast furnace. Powder Technology, 2017, 314: 542–549.

[20] Kurosawa H., Matsuhashi S., Natsui S., Kon T., Ueda S., Inoue R., Ariyama T., DEM-CFD model considering softening behavior of ore particles in cohesive zone and

gas flow analysis at low coke rate in blast furnace. ISIJ International, 2012, 52: 1010–1017.

[21] Li C., Zhang Y., Shen J., Zhang W., Coupled simulation of fluid-particle interaction for large complex granules: A resolved CFD-DEM method for modelling the airflow in a vertical fixed bed of irregular sinter particles. Particuology, 2024, 90: 292–306.

[22] Shen Y., Zheng B., Sun P., Qi C., Wang M., Dong Y., Wang Y., Lv J., Wang Y., Effects of ellipsoidal and regular hexahedral particles on the performance of the waste heat recovery equipment in a methanol reforming hydrogen production system. International Journal Hydrogen Energy, 2023, 48: 11141–11152.

[23] Feng Y.H., Zhang Z., Qiu L., Zhang X.X., Heat recovery process modelling of semi-molten blast furnace slag in a moving bed using XDEM. Energy, 2019, 186: 115876.

[24] Zhang S., Zhao L., Feng J., Dong H., Numerical investigation of the air-particles heat transfer characteristics of moving bed—Effect of particle size distribution. International Journal of Heat and Mass Transfer, 2022, 182: 122036.

[25] Qiu L., Sang D., Li Y., Feng Y., Zhang X., Numerical simulation of gas-solid heat transfer characteristics of porous structure composed of high-temperature particles in moving bed. Applied Thermal Engineering, 2020, 181: 115925.

[26] Yang W.J., Zhou Z.Y., Yu A.B., Particle scale studies of heat transfer in a moving bed. Powder Technology, 2015, 281: 99–111.

[27] Morris A.B., Ma Z., Pannala S., Hrenya C.M., Simulations of heat transfer to solid particles flowing through an array of heated tubes. Solar Energy, 2016, 130: 101–115.

[28] Lu W., Ma C., Liu D., Zhao Y., Ke X., Zhou T., A comprehensive heat transfer prediction model for tubular moving bed heat exchangers using CFD-DEM: Validation and sensitivity analysis. Applied Thermal Engineering, 2024. 247: 123072.

[29] ANSYS Inc., ANSYS Fluent Theory Guide Release 2022 R1, Southpointe. 2600 Ansys Drive Canonsburg, PA 15317, USA, 2022.

[30] Ding J., Gidaspow D., A bubbling fluidization model using kinetic theory of granular flow. AIChE Journal, 1990, 36: 523–538.

[31] DEM Solutions Ltd., EDEM 2020.2 Documentation, Edinburgh, UK, 2020.

[32] Van Antwerpen W., Rousseau P.G., Du Toit C.G., Multi-sphere unit cell model to calculate the effective thermal conductivity in packed pebble beds of mono-sized spheres. Nuclear Engineering and Design, 2012, 247: 183–201.

[33] Wang Z., Liu M., Semi-resolved CFD-DEM for thermal particulate flows with applications to fluidized beds. International Journal of Heat and Mass Transfer, 2020, 159: 120150.

[34] Xiao P.H., Li B.W., Sun Y.S., A model to determine the overall bed-to-wall heat transfer coefficient and its influence factor analysis in moving bed. International Journal of Heat and Mass Transfer, 2020, 154:119655.

[35] Wu W.Y., Liu X.J., Liang X., Xia D.H., Operation characteristics of waste heat recovery from high-temperature particles under varying temperatures and flow rates. International Journal of Thermal Sciences, 2022, 172: 107283.

[36] Dinghe L., Tuo Z., Baoguo F., Ruibin S., Zepeng L., Experimental measurement and analysis of thermal physical parameters of sinter and pellet. Metallurgical Power, 2021, 253: 93–97.

[37] Zhang R., Yang H., Lu J.F., Wu Y., Theoretical and experimental analysis of bed-to-wall heat transfer in heat recovery processing. Powder Technology, 2013, 249: 186–195.

[38] Bartsch P., Zunft S., Granular flow around the horizontal tubes of a particle heat exchanger: DEM-simulation and experimental validation. Solar Energy, 2019, 182: 48–56.

[39] Oka Y.I., Mihara S., Yoshida T., Impact-angle dependence and estimation of erosion damage to ceramic materials caused by solid particle impact. Wear, 2009, 267: 129–135.